ACS Energy LETTERS

http://pubs.acs.org/journal/aelccp

LETTER

Two Regimes of Bandgap Red Shift and Partial Ambient Retention in Pressure-Treated Two-Dimensional Perovskites

HPSTAR 448-2017

Gang Liu,*[,†,‡] Lingping Kong,[†,‡] Peijun Guo,[§] Constantinos C. Stoumpos,[∥] Qingyang Hu,[†] Zhenxian Liu,[‡] Zhonghou Cai,[⊥] David J. Gosztola,[§] Ho-kwang Mao,*[,†,‡] Mercouri G. Kanatzidis,[∥] and Richard D. Schaller*[,§,∥]

[†]Center for High Pressure Science and Technology Advanced Research, Shanghai 201203, China
[‡]Geophysical Laboratory, Carnegie Institution of Washington, Washington, DC 20015, United States
[§]Center for Nanoscale Materials, Argonne National Laboratory, Argonne, Illinois 60439, United States
[∥]Department of Chemistry, Northwestern University, 2145 Sheridan Road, Evanston, Illinois 60208, United States
[⊥]Advanced Photon Source, Argonne National Laboratory, Argonne, Illinois 60439, United States

Supporting Information

ABSTRACT: The discovery of elevated environmental stability in two-dimensional (2D) Ruddlesden–Popper hybrid perovskites represents a significant advance in low-cost, high-efficiency light absorbers. In comparison to 3D counterparts, 2D perovskites of organo-lead-halides exhibit wider, quantum-confined optical bandgaps that reduce the wavelength range of light absorption. Here, we characterize the structural and optical properties of 2D hybrid perovskites as a function of hydrostatic pressure. We observe bandgap narrowing with pressure of 633 meV that is partially retained following pressure release due to an atomic reconfiguration mechanism. We identify two distinct regimes of compression dominated by the softer organic and less compressible inorganic sublattices. Our findings, which also include PL enhancement, correlate well with density functional theory calculations and establish structure–property relationships at the atomic scale. These concepts can be expanded into other hybrid perovskites and suggest that pressure/strain processing could offer a new route to improved materials-by-design in applications.

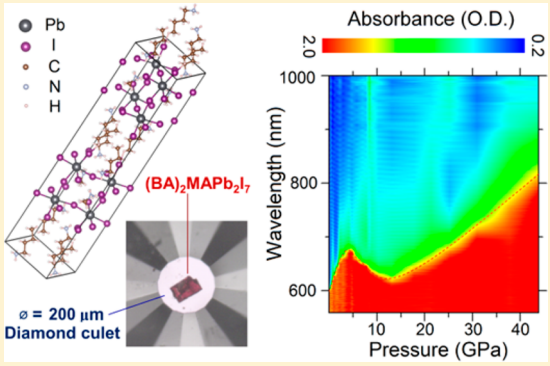

Over the past several years, phenomenal advances in photovoltaic (PV) and optoelectronic devices appeared owing to organic–inorganic hybrid perovskites with such materials now positioned to provide some of the highest-performance, lowest-cost options for future clean energy generation.[1−4] Three-dimensional (3D) perovskites (such as methylammonium lead iodide, $MAPbI_3$) have gained a key position among light absorber candidates due to their unique physical properties (for example, strong integrated solar absorption, nearly optimal bandgap based on the Shockley–Queisser Limit, and long carrier diffusion length).[5−8] Currently, $MAPbI_3$-based single-junction solar cells have achieved a power conversion efficiency of 22.1%.[2] However, further developments of 3D perovskites seemingly suffer from a dilemma between high performance and instability issues. Although many attempts have been made to partially alleviate the instabilities caused by moisture, oxygen, light illumination, and applied fields,[9,10] a widely observed self-degradation mechanism induced by iodine vapor loss under working conditions was recently suggested;[11] thus, other chemical variants or altered dimensionality perovskites (beyond 3D) are urgently needed for stable, long-term PV and optoelectronic applications.

Two-dimensional (2D) hybrid perovskites incorporate organic interlayers and inorganic sheets with each other, reminiscent of a natural multiquantum well structure.[12−14] These 2D hybrid perovskites, in which carriers and mobile ions are confined within the inorganic network, offer significantly improved stability to various environmental triggers. Kanatzidis et al. synthesized 2D Ruddlesden–Popper perovskites $(BA)_2(MA)_{n-1}Pb_nI_{3n+1}$, where anionic $((MA)_{n-1}Pb_nI_{3n+1})^{2-}$ are isolated by organic *n*-butylammonium (BA) groups, and achieved a PV efficiency of 12.52% in encapsulated solar cells

Received: August 28, 2017
Accepted: October 3, 2017
Published: October 3, 2017

© XXXX American Chemical Society

DOI: 10.1021/acsenergylett.7b00807
ACS Energy Lett. 2017, 2, 2518−2524

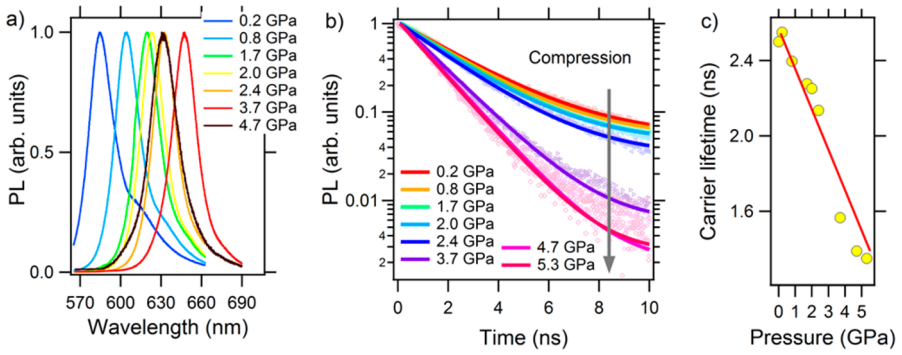

Figure 1. In situ high-pressure PL and TRPL characterizations on $(BA)_2(MA)Pb_2I_7$. (a) Pressure-dependent static PL signal in compression. In this panel, the traces are normalized by the maximum PL intensity. (b) High-pressure TRPL measurements (dots) and single-exponential fits (lines) on a $(BA)_2(MA)Pb_2I_7$ sample, normalized at 0 ns. (c) Pressure dependence of the fitted carrier lifetime. The symbol size relates the size of the fit error bars.

without any degradation over 2250 h under AM1.5G illumination or 65% relative humidity.[13] In order to improve the device performance further, it is highly desirable to tune the hybrid perovskites so as to increase visible and near-infrared light absorption.[15,16] The Shockley−Queisser limit for single-junction solar cells requires an optimum bandgap energy of 1.3−1.5 eV,[5] obviously smaller than that of the as-prepared pristine 2D perovskites $(BA)_2(MA)_{n-1}Pb_nI_{3n+1}$ (2.43 eV for $(BA)_2PbI_4$; 2.17 eV for $(BA)_2(MA)Pb_2I_7$).[14,17] Here, we employ hydrostatic pressure as an effective and clean tool[18−20] to precisely manipulate the structural and electronic properties of 2D perovskites in a controlled manner, to reveal a consecutive structure−property relationship in a pure phase that cannot readily be obtained by chemical modification methods. We first observed pressure-driven, highly tunable light absorption with a 633 meV red shift in the absorption edge, attributing it to unique "two-step" structural compression behavior in 2D layered perovskites. More interestingly, for the decompressed 2D perovskites, we obtained a desirable narrower bandgap and enhanced photoluminescence (PL) without sacrificing good stability. Therefore, our study paves the way to produce new properties in known 2D perovskites for highly efficient PV and optoelectronic applications.

A structural illustration of the layered perovskites $(BA)_2(MA)Pb_2I_7$ (Figure S1) shows inorganic layers of corner-sharing octahedral $[PbI_6]^{4-}$ units filled in between interdigitating bilayers of inserted bulky $[BA]^+$ spacer cations. High-resolution X-ray diffraction (XRD) examined the crystal structure of the $(BA)_2(MA)Pb_2I_7$ samples used in this study under ambient pressure conditions, and the results (Figure S2 and Table S1) confirm a *Cc2m* space group with corresponding lattice parameters (a = 9.0184(2) Å, b = 39.598(3) Å, c = 8.9323(2) Å), in good agreement with previous reports.[17] Optical absorption and PL spectra (Figures S3 and S4) show an excitonic transition centered at 587 nm and a direct bandgap of 2.053 eV, which are blue-shifted by 203 nm and 516 meV as compared to those of the bulk $MAPbI_3$, respectively. These blue shifts are consistent with the dimensional reduction and corresponding quantum confinement effects. Time-resolved photoluminescence (TRPL) decays (Figure S5) reveal single-exponential decays with a lifetime of 2.50 ± 0.01 ns and are of the same order as the bromine-based 2D perovskite BA_2PbBr_4 (3.3 ns).[12]

We performed in situ high-pressure PL and TRPL (Figure 1) to explore optoelectronic properties including light emission and carrier recombination behavior of $(BA)_2(MA)Pb_2I_7$ under compression. Figure 1a shows a pronounced red shift of the PL peak position from 587 nm at ambient pressure to 648 nm at 3.7 GPa and then a blue shift up to 631 nm at 4.7 GPa, suggesting a trend of bandgap narrowing followed by widening upon compression. For in situ high-pressure TRPL measurements, the data were collected at the wavelength of the respective main pressure-dependent static PL peaks. As shown in Figure 1b,c, the PL decay rate increased monotonically as pressure increased. This pressure-dependent PL decay rate may arise from two effects. Electron−phonon scattering is expected to be more significant at high pressure because of the deformation potential contribution due to atomic displacement (crystalline to noncrystalline transition; the break of the translational symmetry or distortion in atomic position).[21,22] We observed a sizable drop in the carrier lifetime between 2.4 and 3.7 GPa (Figure 1c), where an obvious atomic distortion occurred as revealed by in situ synchrotron XRD results discussed later. Also, an increased spatial overlap of the electron and hole wave functions composed of the respective Pb 6p and I 5s is expected to occur at higher pressures, which can be responsible for an enhanced emission rate.[23] The pressure dependence of the PL intensity (Figure S6) and PL decay can be correlated with the quantum yield (QY) for a constant excitation intensity. At ambient conditions, the magnitude of the QY of $(BA)_2MAPb_2I_7$ was determined to be 4.53%, and then, the pressure dependence of the QY was estimated (Figures S7 and S8a). The QY is related to the radiative decay rate (τ_{rad}) and the nonradiative decay rate (τ_{nrad}) by QY = $\tau_{rad}/(\tau_{rad} + \tau_{nrad})$, from which we calculate the τ_{rad} and τ_{nrad} as a function of pressure for $(BA)_2MAPb_2I_7$ under compression, and then the radiative lifetime and nonradiative lifetime (inverse of decay rate) can be obtained (Figure S8b). The increase of the PL counts from 1 atm to 1.7 GPa (Figure S6) are qualitatively consistent with a decreasing radiative lifetime (growing τ_{rad}), as plotted in Figures S8b. The radiative recombination rate is expected to be influenced by phonon scattering. If the carrier−lattice coupling is strong, the exciton is self-trapped and higher recombination rate occurs; if the carrier−lattice coupling is weak, the exciton is more delocalized and polaron-like, behaving as free quasiparticles, and a lower recombination rate could be expected.[18] On the basis of the results shown in Figure S8b, we believe that the carrier−lattice coupling effect in $(BA)_2MAPb_2I_7$ becomes stronger under compression in the low-pressure range. One can see that the rate of the PL count increase is faster than the rate of the τ_{rad} increase, which demonstrates a decreasing τ_{nrad} (increasing nonradiative

DOI: 10.1021/acsenergylett.7b00807
ACS Energy Lett. 2017, 2, 2518−2524

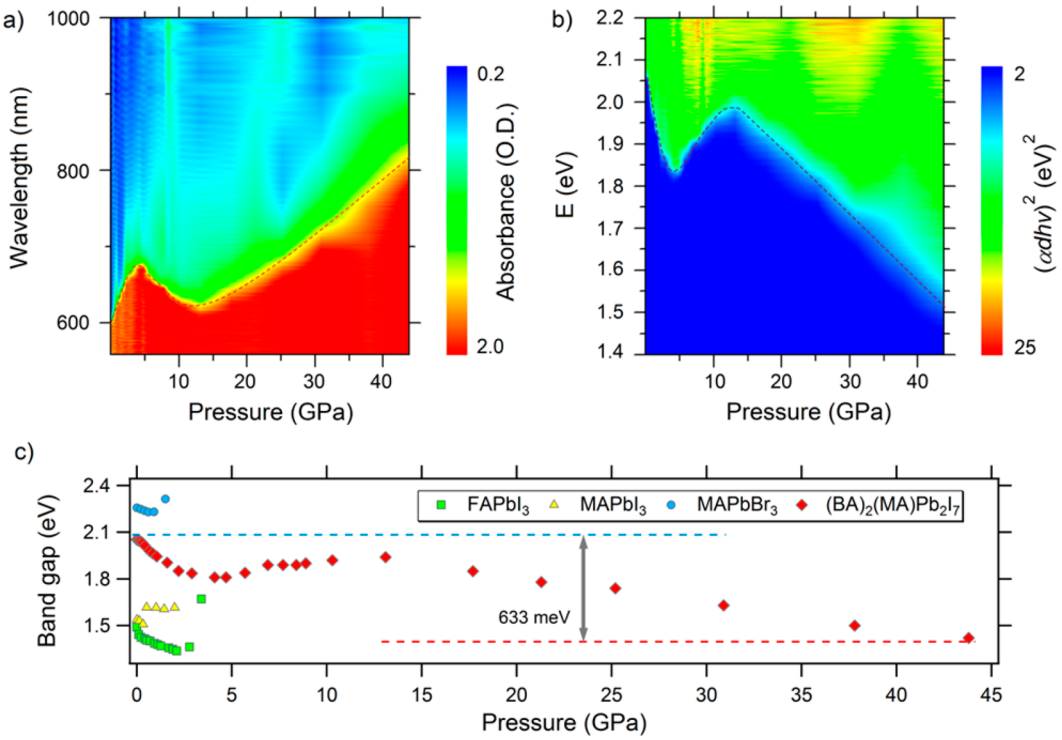

Figure 2. In situ high-pressure optical absorption measurements of $(BA)_2(MA)Pb_2I_7$. (a) Color plots of pressure-dependent optical absorbance spectra. (b) Color plots of pressure-dependent $(\alpha dh\nu)^2$ versus photon energy. (c) Summary of the pressure dependence of the bandgap for various hybrid perovskites. Magnitudes of bandgaps can be estimated by extrapolating the linear portion of the Tauc plots to the baselines. Data are from refs 22 and 24 and this work. The symbol size covers the size of the error bars.

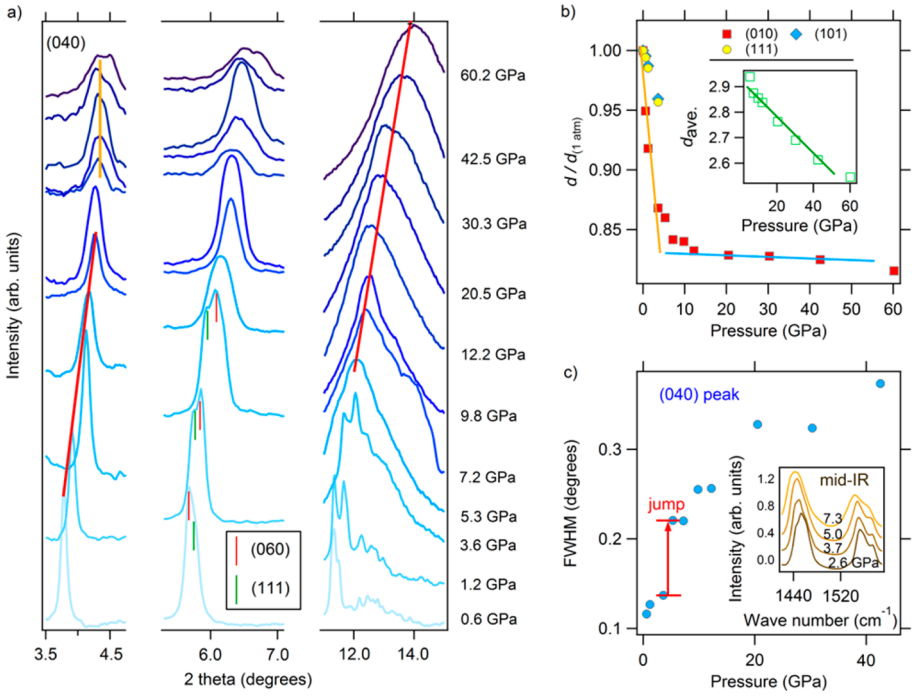

Figure 3. In situ high-pressure structural characterizations on $(BA)_2(MA)Pb_2I_7$. (a) High-pressure synchrotron XRD patterns at various 2 theta ranges. (b) Pressure dependence of the *d*-spacing. Due to the broadened XRD pattern caused by inevitable pressure-driven atomic distortion, we cannot have a detailed structure analysis of the high-pressure structure. However, pressure dependences of the layer-to-layer distance and average lattice constant contributed to by multicrystalline directions can be clearly derived, and then, a two-step compression behavior can be concluded. The inset shows the pressure dependence of d_{ave}. (c) Pressure-induced atomic distortions evidenced by broadened XRD, which can also be suggested by the broadened mid-IR peaks (see inset) at higher pressures. The symbol size covers the size of the error bars.

DOI: 10.1021/acsenergylett.7b00807
ACS Energy Lett. 2017, 2, 2518−2524

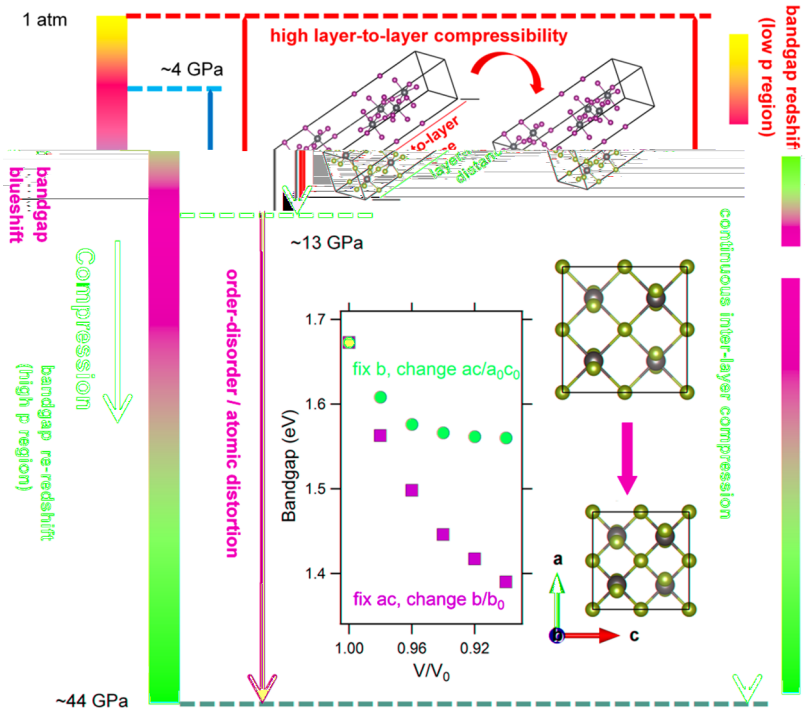

Figure 4. Structural origin of bandgap evolution in compression. The inset in the middle lower part shows the DFT calculation results of pressure-driven bandgap changes (as a function of reduced relative volume) along (010) and (101) directions.

lifetime) as the pressure increases to 1.7 GPa (Figure S8b). In this pressure range, layer-to-layer compression dominates but a minimal order-to-disorder transition takes place. We note that the carriers are mainly scattered by homopolar phonon modes, which are oriented in the out-of-plane direction,[21] which is the direction of the pressure-induced deformation in the low-pressure range. Therefore, the increase of PL counts and the increase of the PL radiative decay rate may be correlated with a stronger scattering of carrier by homopolar phonons with eigenvectors parallel to the direction of the layer-to-layer compression. Further pressure elevation significantly increases the crystalline disorder and likely yields a large τ_{nrad}, thereby quenching the PL.

The pressure-dependent bandgap in 2D perovskites was further investigated by in situ optical absorption spectroscopy under pressures from 1 atm up to 44 GPa (Figure 2). The color-coded, pressure- and wavelength-resolved color plot of absorbance shown in Figure 2a presents a red shift until 4 GPa, followed by a blue shift until 13 GPa, consistent with the PL results shown in Figure 1. The blue jump followed by a red shift in the low-pressure range is commonly found in hybrid perovskites (for example, 0.4 GPa for $MAPbI_3$ and 2.0 GPa for $FAPbI_3$)[22,24] owing to atomic distortion. Notably, however, a second discontinuity is observed at 13 GPa for $(BA)_2(MA)Pb_2I_7$ that so far has been absent in 3D perovskites. This discontinuity, triggering a further re-emergence of red shift ("re-redshift") under higher pressure, is highly relevant for optimal solar spectrum absorption. We estimated the bandgap by extrapolating the linear portion of the $(\alpha d h\nu)^2$ versus the $h\nu$ curve (Figures 2b and S9–S11), where α is the absorption coefficient, d is the sample thickness, and $h\nu$ is the photon energy. As summarized in Figure 2c, the re-emergence of the red shift contributes an unprecedented extension of bandgap narrowing up to −633 meV, demonstrating excellent bandgap tunability in 2D perovskites only, even without any chemical modification.

To investigate the structural root cause of such an abnormal re-redshift found in 2D perovskites, we employed in situ synchrotron high-pressure XRD experiments up to 60 GPa. The pressure-dependent XRD patterns are shown in Figure 3a, in which the Bragg (040) and (111) reflections of $(BA)_2(MA)Pb_2I_7$ can be resolved. Figures 3b and S12 display the pressure-driven relative changes in the d-spacing, demonstrating clear anisotropic compression. Up to 12.2 GPa, the volume collapse was mostly contributed by b-axis shortening, represented by a reduction of the d-spacing for the (040) reflection, where the organic cations dominate the large interlayer spaces. However, the b-axis became much more resistant to higher pressure after 12.2 GPa. From 12.2 to 42.5 GPa, the b-axis shortened by only 0.9% compared to 8.1% of d_{ave} (inset of Figure 3b). Here, d_{ave} is derived from fitting the broad XRD peak at high-2 theta and a high-pressure range (Figure 3a). Considering that in the high-2 theta range there are actually many Bragg peaks, d_{ave} can be viewed as the average lattice constant contributed by multicrystalline directions. Because the b-axis is insensitive to compression at high pressures, we expected that the decrease in d_{ave} and volume collapse primarily originated from interlayer compression. We also noted that the full width at half-maximum (fwhm) of the (040) single peak (Figure 3c) significantly broadened, showing an obvious "jump" between 3.6 and 5.3 GPa, indicating pressure-induced atomic distortion that was further supported by the broadening characteristic in the mid-IR modes at 5 GPa (see the inset of Figure 3c and Figures S13 and S14).

As schematically shown in Figure 4, the pressure-driven structural evolution of 2D $(BA)_2(MA)Pb_2I_7$ can be summarized as a unique two-step behavior accompanied by atomic distortion; namely, the compression is dominated by a layer-to-layer approach at low pressures, while interlayer compression

DOI: 10.1021/acsenergylett.7b00807
ACS Energy Lett. 2017, 2, 2518−2524

dominates in the high-pressure range. Such a structural evolution can be understood from the fact that the organic parts inserted between layers are soft while the inorganic sublattices are less compressible and can be well correlated with bandgap changes. As the pressure increases, the Pb s and I p orbital coupling increases and pushes up the top of the valence band as the antibonding interaction between Pb s and I p orbitals is enhanced. Meanwhile, the bottom of the conduction band is predominantly a nonbonding localized state of Pb p orbitals, which is less sensitive to bond length or pressure, and thus, the net result is bandgap narrowing.[22,24,25] Note that both the layer-to-layer and interlayer compressions contribute to the bandgap narrowing, as evidenced by our first-principles simulation (inset of Figure 4, details in Figures S15–S17) and uniaxial compression experiment (Figure S18). Therefore, the bandgap red shift below 4 GPa and re-redshift after 13 GPa can be understood as the result of layer-to-layer and interlayer compressions, respectively. The blue shift between 4 and 13 GPa can be interpreted as atomic distortion that lowers the lattice symmetry and causes less Pb s and I p orbital coupling, consistent with previous results on 3D perovskites.[22,24,26−29] We note that orientational dynamics of the organic cations have important consequences on the structural and electronic properties of hybrid perovskites because the organic and inorganic parts are strongly linked. Thus, to fully understand the structure−properties relationship, in the future, time-resolved ab initio molecular dynamics (AMID) simulations[30,31] are required to be carried out on the structures of equilibrium and strained 2D layered perovskites as well as their electronic properties.

Because the ambient retainability of pressure-treated materials is vitally important for practical applications, we investigated the structural and optical properties of $(BA)_2(MA)Pb_2I_7$ and explored their environmental stability after pressure was completely removed. By comparing the XRD pattern of a sample before compression and after decompression from 60 GPa (Figure 5a), we discovered that the XRD peaks shifted to a smaller *d*-spacing range after the pressure was totally released, meaning that the reduced lattice dimensions at mild pressure were memorized in the quenched sample. More interestingly, an abrupt change in the intensity of the XRD reflections, including (111) and (040), is observed, evidencing obvious atomic reconfiguration. Our GSAS refinement of the XRD pattern (Figure 5b) found that $(BA)_2(MA)Pb_2I_7$ crystallized in the expected layered perovskite structure after decompression, with an orthorhombic *Cc*2*m* symmetry (a = 8.9203(4) Å, b = 39.324(3) Å, c = 8.9535(3) Å; see Tables S3–S5). We conducted first-principles simulation to distinguish the energetic difference between the ambient ground state and the quenched structure, which have an identical space group but are different in lattice parameters and electronic structures. We calculated the pressure dependence of the energy for both the pressure-treated structure and ground-state structure (Figure S19). The initial structures in the simulation were directly imported from experiments and were relaxed for atomic positions at fixed volumes. At ambient condition, the ground state has a relative larger volume but is more energetically favored. Its enthalpy lowers by 0.45 eV/unit cell compared to the quenched structure. For all high-pressure materials investigations, pressures are used to improve the properties and to tune samples away from their ground states, hoping to reach a metastable state with superior properties that could be preserved. The small enthalpy difference between this

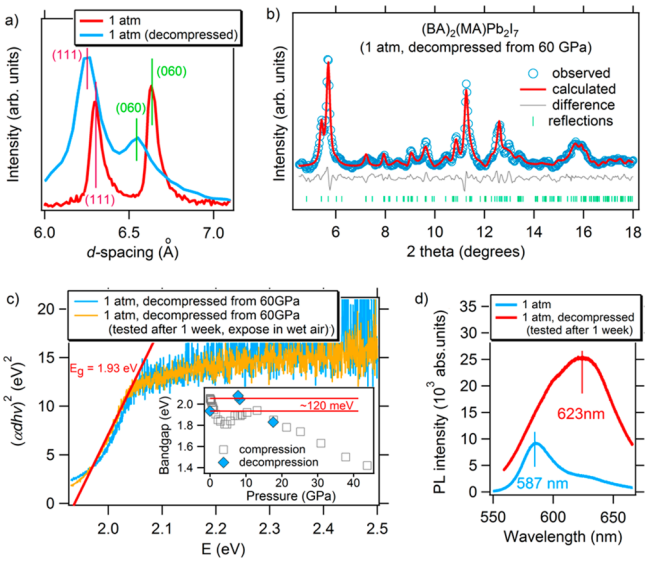

Figure 5. Retainable structural and electronic properties for $(BA)_2(MA)Pb_2I_7$ decompressed from 60 GPa. (a) Noticeable change in relative intensities of (060) and (111) Bragg reflections between the as-prepared sample (before compression) and that decompressed from 60 GPa. (b) XRD pattern and GSAS refinement result of $(BA)_2(MA)Pb_2I_7$. (c) Tauc plots for $(BA)_2(MA)Pb_2I_7$ after compression. Bandgap magnitudes are stable after the sample is exposed to wet air for over 1 week. It can be clearly demonstrated that ~120 meV bandgap narrowing has been achieved in the decompressed sample. (d) Comparison of PL spectra before compression and after decompression. A clear PL enhancement has been confirmed in the decompressed sample.

metastable state and ground state is a great advantage for preserving the metastable state. There must be an energy barrier between these two structures. The magnitude of the energy barrier depends on the detailed path of the structure transition, and a reasonable transition path is related to the high-energy amorphous structure, which has been observed in in situ XRD tests under decompression (Figure S20). Along the pressurization curve, the dense pressure-treated structure becomes more stable at higher pressures. One can see that in the quenched structure from decompression, the Pb−I−Pb angles are closer to 180° than those in the as-prepared sample before compression (Figures S21–S22), enabling a good mixture of the Pb s and I p orbitals. Correspondingly, a narrowed bandgap and broadened visible light absorbance can be expected.[32] Tauc plots shown in Figure 5c for the decompressed $(BA)_2(MA)Pb_2I_7$ demonstrate a direct bandgap of 1.930 eV, which is 123 meV lower than that observed before compression (inset of Figure 5c and Figure S23). Such a pressure-induced contribution is 3 times the magnitude of the highest value reported in 3D hybrid perovskites (ΔE_g = 42 meV for $FAPbI_3$). In addition, the decompressed sample showed no shift for the measured bandgap even after exposure to air (65% relative humidity) for over 1 week, confirming superior moisture tolerance in its optical properties that are rooted in its natural layered structure.[13,14,33] We also discovered that PL enhancement increased by 150% without sacrificing the carrier lifetime in decompressed $(BA)_2(MA)Pb_2I_7$ after the pressure was completely released (Figures 5d and S24). The observed simultaneous characteristics of a narrowed bandgap and strong PL may have applications in field effect transistors, light-emitting diodes, and lasers/detectors.[34] The pressure-treated

DOI: 10.1021/acsenergylett.7b00807
ACS Energy Lett. 2017, 2, 2518−2524

sample size is around 30 μm, which is too small and not enough for real solar cell device fabrication. To have high-performance and large-volume pressurized materials, the use of a large-volume press (LVP) high-pressure facility should be given more attention.[18,35,36]

In conclusion, we conducted the first example of an in situ high-pressure study on the structural and optical properties of 2D Ruddlesden−Popper perovskites. The unique two-step regimes of compression behavior have never been reported in 3D perovskites[22,24,26−29,37] and 2D transition metal dichalcogenides.[38] Our study offers further steps toward tailoring the optoelectronic properties of 2D hybrid perovskites and paves the way for better solar absorbers. The desired high level of bandgap red shift and PL enhancement in a decompressed sample demonstrates that pressure/strain engineering can be a real possibility for modifying material not only in situ but also ex situ. Further high-pressure investigations on 2D hybrid perovskites may focus on the high-pressure phase characterizations and pressure-driven metallic transitions[18] to access new properties for future energy applications.

■ ASSOCIATED CONTENT

Supporting Information

The Supporting Information is available free of charge on the ACS Publications website at DOI: 10.1021/acsenergylett.7b00807.

Experimental and computational details; additional figures and tables (PDF)

■ AUTHOR INFORMATION

Corresponding Authors

*E-mail: liugang@hpstar.ac.cn (G.L.).
*E-mail: hmao@carnegiescience.edu (H.-k.M.).
*E-mail: schaller@anl.gov (R.D.S.).

ORCID

Peijun Guo: 0000-0001-5732-7061
Constantinos C. Stoumpos: 0000-0001-8396-9578
Mercouri G. Kanatzidis: 0000-0003-2037-4168
Richard D. Schaller: 0000-0001-9696-8830

Notes

The authors declare no competing financial interest.

■ ACKNOWLEDGMENTS

This project was supported by the NSAF (U1530402) and National Science Foundation (CBET-1150617). High-pressure powder structure characterizations were performed at beamline 2-ID-D at APS, Argonne National Laboratory (ANL). The use of APS facilities was supported by the U.S. Department of Energy, Office of Science, Office of Basic Energy Sciences (DE-AC02-06CH11357). Part of this work was performed at the Infrared Lab of the National Synchrotron Light Source (NSLS II), Brookhaven National Laboratory (BNL). Support from ONR (N00014-17-1-2231) is acknowledged. This work was performed, in part, at the Center for Nanoscale Materials, a U.S. Department of Energy Office of Science User Facility, and supported by the U.S. Department of Energy, Office of Science, under Contract No. DE-AC02-06CH11357. The Infrared Lab was supported by the National Science Foundation (EAR 1606856, COMPRES) and DOE/NNSA (DE-NA-0002006, CDAC). First-principles simulation was conducted at the SR16000 supercomputing facilities of the Center for Computational Materials Science of the Institute for Materials Research, Tohoku University.

■ REFERENCES

(1) Kojima, A.; Teshima, K.; Shirai, Y.; Miyasaka, T. Organometal Halide Perovskites as Visible-Light Sensitizers for Photovoltaic Cells. *J. Am. Chem. Soc.* **2009**, *131*, 6050−6051.

(2) Saliba, M.; Matsui, T.; Seo, J.-Y.; Domanski, K.; Correa-Baena, J.-P.; Nazeeruddin, M. K.; Zakeeruddin, S. M.; Tress, W.; Abate, A.; Hagfeldt, A.; et al. Cesium-Containing Triple Cation Perovskite Solar Cells: Improved Stability, Reproducibility and High Efficiency. *Energy Environ. Sci.* **2016**, *9*, 1989−1997.

(3) Giustino, F.; Snaith, H. J. Toward Lead-Free Perovskite Solar Cells. *ACS Energy Lett.* **2016**, *1*, 1233−1240.

(4) Green, M. A.; Bremner, S. P. Energy Conversion Approaches and Materials for High-Efficiency Photovoltaics. *Nat. Mater.* **2016**, *16*, 23−34.

(5) Shockley, W.; Queisser, H. J. Detailed Balance Limit of Efficiency of p-n Junction Solar Cells. *J. Appl. Phys.* **1961**, *32*, 510−519.

(6) Nie, W.; Tsai, H.; Asadpour, R.; Blancon, J.-C.; Neukirch, A. J.; Gupta, G.; Crochet, J. J.; Chhowalla, M.; Tretiak, S.; Alam, M. A.; et al. High-Efficiency Solution-Processed Perovskite Solar Cells with Millimeter-Scale Grains. *Science* **2015**, *347*, 522−525.

(7) Wright, A. D.; Verdi, C.; Milot, R. L.; Eperon, G. E.; Pérez-Osorio, M. A.; Snaith, H. J.; Giustino, F.; Johnston, M. B.; Herz, L. M. Electron-Phonon Coupling in Hybrid Lead Halide Perovskites. *Nat. Commun.* **2016**, *7*, 11755.

(8) Zhumekenov, A. A.; Saidaminov, M. I.; Haque, M. A.; Alarousu, E.; Sarmah, S. P.; Murali, B.; Dursun, I.; Miao, X. H.; Abdelhady, A. L.; Wu, T.; et al. Formamidinium Lead Halide Perovskite Crystals with Unprecedented Long Carrier Dynamics and Diffusion Length. *ACS Energy Lett.* **2016**, *1*, 32−37.

(9) Zhou, H.; Chen, Q.; Li, G.; Luo, S.; Song, T. B.; Duan, H. S.; Hong, Z.; You, J.; Liu, Y.; Yang, Y. Interface Engineering of Highly Efficient Perovskite Solar Cells. *Science* **2014**, *345*, 542−546.

(10) Yang, S.; Wang, Y.; Liu, P.; Cheng, Y. B.; Zhao, H. J.; Yang, H. G. Functionalization of Perovskite Thin Films with Moisture-Tolerant Molecules. *Nat. Energy* **2016**, *1*, 15016.

(11) Wang, S.; Jiang, Y.; Juarez-Perez, E. J.; Ono, L. K.; Qi, Y. Accelerated Degradation of Methylammonium Lead Iodide Perovskites Induced by Exposure to Iodine Vapour. *Nat. Energy* **2016**, *2*, 16195.

(12) Dou, L.; Wong, A. B.; Yu, Y.; Lai, M.; Kornienko, N.; Eaton, S. W.; Fu, A.; Bischak, C. G.; Ma, J.; Ding, T.; et al. Atomically Thin Two-Dimensional Organic-Inorganic Hybrid Perovskites. *Science* **2015**, *349*, 1518−1521.

(13) Tsai, H.; Nie, W.; Blancon, J. C.; Stoumpos, C. C.; Asadpour, R.; Harutyunyan, B.; Neukirch, A. J.; Verduzco, R.; Crochet, J. J.; Tretiak, S.; et al. High-Efficiency Two-Dimensional Ruddlesden−Popper Perovskite Solar Cells. *Nature* **2016**, *536*, 312−317.

(14) Cao, D. H.; Stoumpos, C. C.; Farha, O. K.; Hupp, J. T.; Kanatzidis, M. G. 2D Homologous Perovskites as Llight-Absorbing Materials for Solar Cell Applications. *J. Am. Chem. Soc.* **2015**, *137*, 7843−7850.

(15) Hao, F.; Stoumpos, C. C.; Cao, D. H.; Chang, R. P. H.; Kanatzidis, M. G. Lead-free Solid-State Organic-Inorganic Halide Perovskite Solar Cells. *Nat. Photonics* **2014**, *8*, 489−494.

(16) Jeon, N. J.; Noh, J. H.; Yang, W. S.; Kim, Y. C.; Ryu, S.; Seo, J.; Seok, S. I. Solvent Engineering for High-Performance Inorganic-Organic Hybrid Perovskite Solar Cells. *Nature* **2015**, *517*, 476−480.

(17) Stoumpos, C. C.; Cao, D. H.; Clark, D. J.; Young, J.; Rondinelli, J. M.; Jang, J. I.; Hupp, J. T.; Kanatzidis, M. G. Ruddlesden-Popper Hybrid Lead Iodide Perovskite 2D Homologous Semiconductors. *Chem. Mater.* **2016**, *28*, 2852−2867.

(18) Jaffe, A.; Lin, Y.; Karunadasa, H. I. Halide Perovskites under Pressure: Accessing New Properties through Lattice Compression. *ACS Energy Lett.* **2017**, *2*, 1549−1555.

(19) Postorino, P.; Malavasi, L. Pressure-Induced Effects in Organic-Inorganic Hybrid Perovskites. *J. Phys. Chem. Lett.* **2017**, *8*, 2613−2622.

DOI: 10.1021/acsenergylett.7b00807
ACS Energy Lett. 2017, 2, 2518−2524

(20) Szafrański, M.; Katrusiak, A. Photovoltaic Hybrid Perovskites under Pressure. *J. Phys. Chem. Lett.* **2017**, *8*, 2496−2506.
(21) Guo, Z.; Wu, X.; Zhu, T.; Zhu, X.; Huang, L. Electron-Phonon Scattering in Atomically Thin 2D Perovskites. *ACS Nano* **2016**, *10*, 9992−9998.
(22) Kong, L.; Liu, G.; Gong, J.; Hu, Q.; Schaller, R. D.; Dera, P.; Zhang, D.; Liu, Z.; Yang, W.; Zhu, K.; et al. Simultaneous Band-Gap Narrowing and Carrier-Lifetime Prolongation of Organic−Inorganic Trihalide Perovskites. *Proc. Natl. Acad. Sci. U. S. A.* **2016**, *113*, 8910−8915.
(23) Chang, A. Y.; Cho, Y. J.; Chen, K. C.; Chen, C. W.; Kinaci, A.; Diroll, B. T.; Wagner, M. J.; Chan, M. K. Y.; Lin, H. W.; Schaller, R. D. Slow Organic-to-Inorganic Sub-Lattice Thermalization in Methylammonium Lead Halide Perovskites Observed by Ultrafast Photoluminescence. *Adv. Energy Mater.* **2016**, *6*, 1600422.
(24) Liu, G.; Kong, L.; Gong, J.; Yang, W.; Mao, H.-k.; Hu, Q.; Liu, Z.; Schaller, R. D.; Zhang, D.; Xu, T. Pressure-Induced Bandgap Optimization in Lead-Based Perovskites with Prolonged Carrier Lifetime and Ambient Retainability. *Adv. Funct. Mater.* **2017**, *27*, 1604208.
(25) Yin, W.-J.; Yang, J.-H.; Kang, J.; Yan, Y.; Wei, S.-H. Halide Perovskite Materials for Solar Cells: a Theoretical Review. *J. Mater. Chem. A* **2015**, *3*, 8926−8942.
(26) Wang, Y.; Lü, X.; Yang, W.; Wen, T.; Yang, L.; Ren, X.; Wang, L.; Lin, Z.; Zhao, Y. Pressure-Induced Phase Transformation, Reversible Amorphization, and Anomalous Visible Light Response in Organolead Bromide Perovskite. *J. Am. Chem. Soc.* **2015**, *137*, 11144−11149.
(27) Jiang, S.; Fang, Y.; Li, R.; Xiao, H.; Crowley, J.; Wang, C.; White, T. J.; Goddard, W. A., III; Wang, Z.; Baikie, T.; et al. Pressure-Dependent Polymorphism and Band-Gap Tuning of Methylammonium Lead Iodide Perovskite. *Angew. Chem., Int. Ed.* **2016**, *55*, 6540−6544.
(28) Jaffe, A.; Lin, Y.; Beavers, C. M.; Voss, J.; Mao, W. L.; Karunadasa, H. I. High-pressure Single-Crystal Structures of 3D Lead-Halide Hybrid Perovskites and Pressure Effects on Their Electronic and Optical Properties. *ACS Cent. Sci.* **2016**, *2*, 201−209.
(29) Wang, L.; Wang, K.; Xiao, G.; Zeng, Q.; Zou, B. Pressure-Induced Structural Evolution and Band Gap Shifts of Organometal Halide Perovskite-Based Methylammonium Lead Chloride. *J. Phys. Chem. Lett.* **2016**, *7*, 5273−5279.
(30) Mosconi, E.; De Angelis, F. Mobile Ions in Organohalide Perovskites: Interplay of Electronic Structure and Dynamics. *ACS Energy Lett.* **2016**, *1*, 182−188.
(31) Quarti, C.; Mosconi, E.; De Angelis, F. Structural and Electronic Properties of Organo-Halide Hybrid Perovskites from ab initio Molecular Dynamics. *Phys. Chem. Chem. Phys.* **2015**, *17*, 9394.
(32) Stoumpos, C. C.; Kanatzidis, M. G. The Renaissance of Halide Perovskites and Their Evolution as Emerging Semiconductors. *Acc. Chem. Res.* **2015**, *48*, 2791−2802.
(33) Daub, M.; Hillebrecht, H. Synthesis, Single-Crystal Structure and Characterization of $(CH_3NH_3)_2Pb(SCN)_2I_2$. *Angew. Chem., Int. Ed.* **2015**, *54*, 11016−11017.
(34) Kamminga, M. E.; Fang, H. H.; Filip, M. R.; Giustino, F.; Baas, J.; Blake, G. R.; Loi, M. A.; Palstra, T. T. Confinement Effects in Low-Dimensional Lead Iodide Perovskite Hybrids. *Chem. Mater.* **2016**, *28*, 4554−4562.
(35) Wang, Y.; Rivers, M.; Sutton, S.; Nishiyama, N.; Uchida, T.; Sanehira, T. The Large-Volume High-Pressure Facility at GSECARS: A "Swiss-Army-Knife" Approach to Synchrotron-Based Experimental Studies. *Phys. Earth Planet. Inter.* **2009**, *174*, 270−281.
(36) Guignard, J.; Crichton, W. A. The Large Volume Press Facility at ID06 Beamline of the European Synchrotron Radiation Facility as a High Pressure-High Temperature Deformation Apparatus. *Rev. Sci. Instrum.* **2015**, *86*, 085112.
(37) Lü, X.; Wang, Y.; Stoumpos, C. C.; Hu, Q.; Guo, X.; Chen, H.; Yang, L.; Smith, J. S.; Yang, W.; Zhao, Y.; et al. Enhanced Structural Stability and Photo Responsiveness of $CH_3NH_3SnI_3$ Perovskite via Pressure-Induced Amorphization and Recrystallization. *Adv. Mater.* **2016**, *28*, 8663−8668.
(38) Zhao, Z.; Zhang, H.; Yuan, H.; Wang, S.; Lin, Y.; Zeng, Q.; Xu, G.; Liu, Z.; Solanki, G. K.; Patel, K. D.; et al. Pressure Induced Metallization with Absence of Structural Transition in Layered Molybdenum Diselenide. *Nat. Commun.* **2015**, *6*, 7312.

DOI: 10.1021/acsenergylett.7b00807
ACS Energy Lett. 2017, 2, 2518−2524